

Full Length Article

Effects of ambient pressure on ignition and flame characteristics in diesel spray combustion

Kar Mun Pang^{a,*}, Mehdi Jangi^b, Xue-Song Bai^c, Jesper Schramm^a, Jens Honore Walther^{a,d}, Peter Glarborg^e

^a Department of Mechanical Engineering, Technical University of Denmark, 2800 Kgs. Lyngby, Denmark

^b Department of Mechanical Engineering, University of Birmingham, B15 2TT Birmingham, UK

^c Department of Energy Sciences, Lund University, 22100 Lund, Sweden

^d Computational Science and Engineering Laboratory, ETH Zürich, CH-8092 Zürich, Switzerland

^e Department of Chemical and Biochemical Engineering, Technical University of Denmark, 2800 Kgs. Lyngby, Denmark

ARTICLE INFO

Keywords:

Spray flame

Transported probability density function

Ignition

Pressure effects

ABSTRACT

This work reports on numerical investigation of effects of ambient pressure (P_{am}) on spray combustion under engine-like conditions. Three cases with different P_{am} of 42, 85 and 170 bar at a fixed ambient temperature of 1000 K are considered. Zero-dimensional calculations are first performed for autoignition of stagnant adiabatic homogenous mixtures to evaluate performance of the selected diesel surrogate fuel models and to identify the P_{am} effects on the most reactive mixture. An Eulerian-based transported probability density function model is then chosen for the three-dimensional computational fluid dynamics study. The results show the predicted ignition delay times and flame lift-off lengths are in reasonably good agreement with experiment, with the relative difference below 28%. The current work reveals that low-temperature reactions occur across a wide range of mixture fraction but a noticeable rise of temperature (> 100 K above ambient temperature) is detected first on the fuel-lean side of the stoichiometric line in all three cases. The high-temperature ignition occurs first on the fuel-rich side in the 42 and 85 bar cases, where the igniting mixture appears to be more fuel-rich in the latter case. As P_{am} is further increased to 170 bar, the igniting mixture becomes more fuel-lean and the high-temperature ignition occurs on the fuel-lean side. The ignition behavior is found to depend on both physical and chemical processes. At 170 bar, the reaction rate increases and the associated transition from low- to high-temperature ignition is relatively fast, as compared to the transport of warmer products from the lean zone into the fuel-rich mixture. Also, within the fuel-rich region, the local temperature is low due to liquid fuel vaporization and the condition is not appropriate for ignition. These collectively cause the high-temperature ignition to occur on the fuel-lean side. Analyses on the quasi-steady spray flame structures reveal that, apart from poorer air entrainment due to reduced lift-off length, the higher rich-zone temperature and lower scalar dissipation rate also lead to a higher peak soot volume fraction at higher P_{am} .

1. Introduction

Over the last few decades, automotive, light-duty, heavy-duty and marine engine industries have been working on improving the understanding of in-cylinder phenomena, which is an important prerequisite to design clean and efficient engines [1–12]. Numerous research groups, mainly led by the Sandia National Laboratory, share their optical measurements and modelling results through the Engine Combustion Network (ECN) [3], with the aim to facilitate and consolidate diesel spray combustion research. Effects of a wide range of diesel engine parameters on fuel penetration, ignition delay time (IDT), flame

lift-off length (LOL) and soot volume fraction ($f_{v,soot}$) have been studied. However, the majority of these studies were performed for an ambient density (ρ_{am}) range of 14.8–22.8 kg/m³. In particular, the Spray A condition, where ρ_{am} is fixed at 22.8 kg/m³ has been broadly studied in the last couple of years, with an emphasis on understanding the ignition and flame stabilization processes [4–7]. The initial ambient air temperature before the air is cooled by the vaporized fuel, T_{am} , is set to 900 K, corresponding to an ambient pressure (P_{am}) of ~ 67 bar. Under the typical range of T_{am} at the start of injection in heavy-duty and large two-stroke marine engines, the ambient densities can be approximately 30.0 and 60.0 kg/m³ under part and full load conditions, respectively

* Corresponding author.

E-mail address: kmpan@mek.dtu.dk (K.M. Pang).

<https://doi.org/10.1016/j.fuel.2018.10.020>

Received 17 April 2018; Received in revised form 2 October 2018; Accepted 3 October 2018

0016-2361/ © 2018 Elsevier Ltd. All rights reserved.

[10,12–15]. Optical accessible experiments conducted at such a high P_{am} (or P_{am}) were reported by Siebers and co-workers [8–12]. In their experimental studies, the P_{am} was varied from 7.3 to 58.5 kg/m³, corresponding to a P_{am} of ~20 to ~170 bar at a T_{am} of 1000 K. Under these test conditions, both the liquid and vapor penetration lengths decreased with increasing P_{am} . Besides that, IDT and flame LOL were found to decrease with increasing P_{am} , while the spray flame size at quasi-steady state (in terms of both length and width) reduced when P_{am} increased [10,11]. The effects of P_{am} on ignition and premixed combustion processes up to 45.0 kg/m³ (~120 bar at T_{am} of 1000 K) were also investigated by Higgins et al. [12]. In terms of soot formation, measurements from optical accessible experiments showed path-length-averaged $f_{v,soot}$ and maximum $f_{v,soot}$ increased with P_{am} [3,13]. Nevertheless, it is challenging to deduce the low- and high-temperature ignition as well as other combustion phenomena solely based on experimental observation at such elevated P_{am} . To date, the effects of P_{am} on spray flame structures under these conditions were not explicitly studied numerically, although these experimental data have been used for computational fluid dynamic (CFD) model validation [16,17]. A more comprehensive understanding of P_{am} effects is crucial for both modelling of engine combustion and for developing physical and chemical models at these P_{am} levels.

Set against this background, the objectives of this CFD work are first to generate velocity, species and temperature distribution profiles to help improving the understanding of the ignition/combustion process at high P_{am} levels; and second to elucidate the effects of P_{am} on spray flame structure and emissions formation. These aims are achieved by employing an Eulerian-based transported probability density function (PDF) method [18] and a skeletal *n*-heptane mechanism [19]. Zero-dimensional calculations are also performed for autoignition of stagnant adiabatic homogenous mixtures to complement the CFD study.

The remainder of the paper is structured as follows. In the next section, experimental data used for model validation are first described. It is followed by the descriptions of the numerical methods. The subsequent sections detail the model validation as well as the numerical analyses of autoignition and flame structures at different P_{am} levels. Conclusions from this work are outlined in the final section.

2. Experimental data for model validation

The grade number two diesel fuel (diesel #2) spray experimental data used for model validation in this work were obtained in a constant volume pre-burn chamber [9,10]. The initial ambient gas composition is determined by the composition of the combustible-gas mixture burned to generate diesel engine-like temperatures and pressures. In the selected test conditions, the reaction $3.245\text{C}_2\text{H}_2 + 0.515\text{H}_2 + 8.37\text{O}_2 + 89.75\text{N}_2 \rightarrow 89.75\text{N}_2 + 6.49\text{CO}_2 + 3.76\text{H}_2\text{O}$ was used to generate the inert high-pressure, high-temperature environment in the non-reacting spray cases. A combustible-gas mixture of 68.1% N₂, 28.4% O₂, 3.0% C₂H₂ and 0.5% H₂ (by volume) was then used in the reacting spray cases. The product composition of this combustible mixture simulated air, having a composition of 21.0% O₂, 69.3% N₂, 6.1% CO₂, and 3.6% H₂O (by volume) [10–12]. The experimental initial ambient gas composition is used in the current reacting spray cases in order to produce identical initial thermochemical conditions. The model performance in simulating fuel penetration lengths of evaporating, non-reacting sprays (cases 1–3 shown in Table 1) at different P_{am} is first evaluated. For liquid-phase, the comparison is made against the liquid penetration length determined with the liquid length scaling law. The properties of *n*-heptadecane are used in the liquid length scaling law to produce diesel #2 liquid length [8] since these resemble the properties of diesel #2. The simulated vapor penetration length is compared with the measurements reported by Naber and Siebers [9]. For the validation of the reacting sprays (cases 4–6 shown in Table 1), IDT and LOL measurements from the ECN database [3] are used; more descriptions can be found in Ref. [10].

As depicted in Table 1, three cases with different ρ_{am} of 14.8, 30.0

Table 1

Operating conditions and injection specifications.

Case	$O_{2,am}$	T_{am} [K]	ρ_{am} (kg/m ³)	D_{nozz} (μm)	P_{inj} (bar)	\dot{m}_f (mg/ms)
1	0	1000	13.9	257	1400	14.0
2	0	1000	28.6	257	1400	14.0
3	0	1000	58.6	257	1400	14.0
4*	21%	1000	14.8	180	1400	8.8
5*	21%	1000	30.0	180	1400	9.0
6*	21%	1000	58.5	180	1400	9.2

* Note: Non-reacting, vaporising spray simulations are also carried out for cases 4–6, where $O_{2,am}$ is set to 0.

and 58.5 kg/m³ are considered for the reacting conditions. At a fixed T_{am} of 1000 K, these correspond to P_{am} of 42, 85 and 170 bar, respectively. Initial species composition, flow and turbulence conditions can be found in a previous work [20]. The operating conditions as well as the injection specifications including nozzle diameter (D_{nozz}), injection pressure (P_{inj}) and fuel mass flow rate (\dot{m}_f) of the test cases are listed in Table 1.

3. Numerical methods

3.1. Autoignition of homogeneous mixtures

To date, effects of P_{am} on autoignition of various hydrocarbon fuels have been studied in shock tube and plug flow reactor experiments as well as kinetic model simulations. Hashemi et al. [21–23] recently studied the effects of P_{am} on C₁–C₃ hydrocarbon reacting pathway up to 100 bar. However, for larger hydrocarbons which are commonly used as diesel #2 surrogate fuels such as *n*-heptane [24,26], *n*-dodecane/myxylene [27] and diesel primary reference fuels [28], the highest P_{am} was only ~50 bar. To the authors' knowledge, validation of diesel #2 surrogate fuel kinetic models for P_{am} levels of 80 bar and above (targeted conditions in the current test cases) is not available. Thus, five different chemical kinetic mechanisms are evaluated at different P_{am} levels. These include the detailed Lawrence Livermore National Laboratory *n*-heptane model (the Mehl654 mechanism) [24] and two of its skeletal versions (the Liu44 and Lu68 mechanisms) [19,25], a recently updated *n*-heptane model (the Zhang1268 mechanism) [26], and an integrated model of *n*-dodecane and myxylene (the Pei163 mechanism) [27]. To evaluate the selected chemical mechanisms, zero-dimensional (0-D) calculations are conducted for autoignition of stagnant adiabatic homogenous mixtures at three different initial P_{am} of 42, 85 and 170 bar using the CHEMKIN-PRO software [29]. The IDT is defined as the time where the mixture temperature increases to 400 K above the initial temperature ($T_{t=0}$). A quadratic relation, $T_{t=0} = T_{am} + 1120Z^2 - 1370Z$, is used to correlate the temperature and mixture fraction. Here, Z is the Bilger mixture fraction while T_{am} is the initial ambient temperature in the combustion chamber and is set to 1000 K. This relation is obtained by post-processing the 3D-CFD results of the reacting case prior to the start of low-temperature ignition, corresponding to the mixing between the cold fuel and hot air. The quadratic relation is constructed for $0 \leq Z \leq 0.4$ and the same function is found applicable to represent the mixing at all three P_{am} (cf. Figs. 7–9) such that P_{am} is the only variable in the comparison. Akin to that in Ref. [30], the most reactive mixture (Z_{mr}) is characterized as the mixture which has the shortest IDT, and the associated IDT can serve as a reference for the comparison against the results from inhomogeneous and turbulent mixtures [30]. It may be worth mentioning that effects of pressure on Z_{mr} have not yet been explicitly studied for turbulent non-premixed flames [31]. Based on the results of Fig. 1, all the models produce similar qualitative trends with respect to the change of P_{am} , i.e., the Z_{mr} occurs in more fuel-lean mixture and Z_{mr} falls closer to the stoichiometric mixture fraction, Z_{st} , when P_{am} increases (cf. Fig. 1). The results also show that the IDT predicted by the Liu44 mechanism is

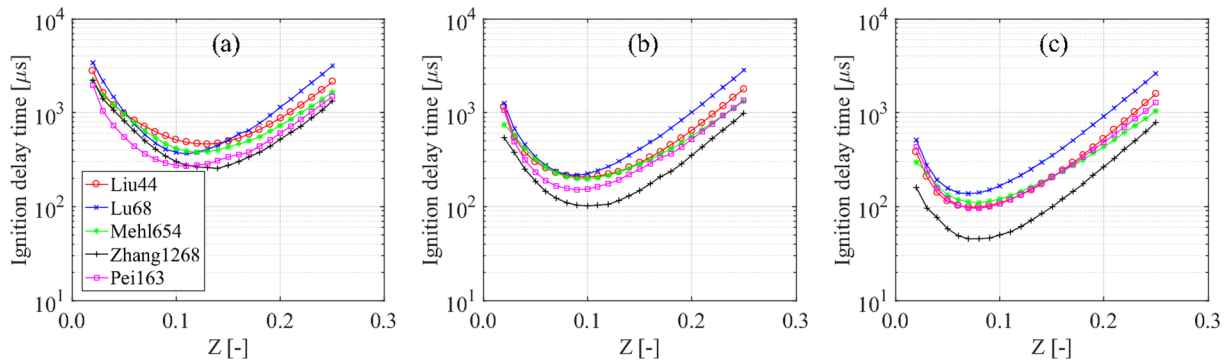


Fig. 1. Ignition delay times of homogenous mixtures for varying initial mixture fraction and temperatures at (a) 42 bar, (b) 85 bar and (c) 170 bar.

close to those of its detailed counterpart, in particular near the Z_{mr} regimes. This trend is similar to that reported by Pei et al. [32] under a similar ambient, thermochemical condition, although the fuel temperature is lower at 373 K in their cases.

In the case where the Liu44 model is used, Z_{mr} are recorded to be 0.13, 0.10 and 0.07 in 42, 85 and 170 bar case, respectively. The corresponding $T_{i=0}$ are 841 K, 874 K and 910 K. The simulated heat-release rate (HRR) profiles are plotted in Fig. 2. Temporal evolution of the heptyl radical (RO_2) of these cases are also provided to indicate the low-temperature ignition. Here, the IDTs coincide at the peaks of the HRR. The IDT can be expressed as $IDT = \tau_{c,1} + \tau_{c,2}$, where $\tau_{c,1}$ and $\tau_{c,2}$ are the first-stage (low-temperature) and second-stage (high-temperature) IDTs, respectively. All the mixtures in these cases undergo two-stage ignition, where the high-temperature ignition occurs after the high amount of RO_2 is consumed. It is also noted in the insets of Fig. 2 that $\tau_{c,2}$ becomes negligible when the P_{am} increases. The Liu44 mechanism is then chosen for the 3-D CFD simulations, which are described in the following section.

3.2. CFD model formulation

The 3-D CFD spray combustion simulations are carried out using OpenFOAM version 3.0.1 [33]. Detailed descriptions of the model can be found in [35] and only a brief description is provided here. The fuel spray, flow and combustion processes are modelled using the Eulerian-Lagrangian approach within the unsteady Reynolds averaged Navier-Stokes (URANS) framework. The Reitz-Diwakar model is used to

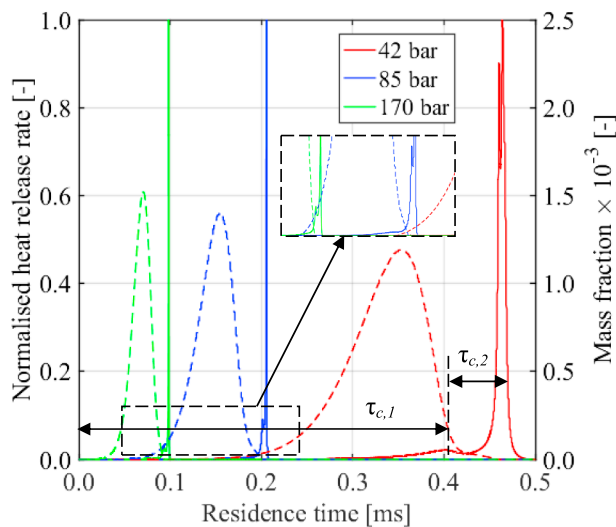


Fig. 2. Ignition histories of Z_{mr} computed in the zero-dimensional homogenous reactor model using the Liu44 mechanism. Solid lines denote the normalized heat release rate while dotted lines represent the mass fraction of RO_2 .

simulate the fuel droplet breakup, while the Realizable $k-\epsilon$ model is employed for turbulence modelling. For the nitric oxide (NO) formation modelling, the Zeldovich thermal NO sub-mechanism from Ref. [34] are added to the Liu44 mechanism. The interaction between turbulence and chemistry is modelled using the Eulerian-based transported PDF method, Eulerian Stochastic Field (ESF) [18]. Similar to the Lagrangian particle transported PDF method, the ESF method is a general approach to account for the turbulence-chemistry interaction (TCI). It can be used to simulate the autoignition as well as different levels of ‘premixedness’ *i.e.*, premixed, partially premixed and non-premixed. In the ESF method, the governing equation for the n -th stochastic field is

$$\begin{aligned} \bar{\rho} d\phi_a^{(n)} = & -\bar{\rho} \tilde{u}_i \frac{\partial \phi_a^{(n)}}{\partial x_i} dt + \bar{\rho} S_{\alpha}^r(\phi^{(n)}) dt + \bar{\rho} S_{\alpha}^s(\phi^{(n)}) dt \\ & + \frac{\partial}{\partial x_i} \left(\Gamma_i \frac{\partial \phi_a^{(n)}}{\partial x_i} \right) dt - \frac{1}{2} \bar{\rho} C_{\phi} (\phi_{\alpha}^{(n)} - \tilde{\phi}_{\alpha}) \omega_i dt + \bar{\rho} \sqrt{2 \frac{\Gamma_i}{\bar{\rho}}} \left(\frac{\partial \phi_a^{(n)}}{\partial x_i} \right) dW_i^{(n)} \end{aligned} \quad (1)$$

where ϕ_a denotes the mass fraction of species (Y_i) or the enthalpy of the mixture (h), and $\phi^{(n)} = [Y_1^{(n)}, Y_2^{(n)}, \dots, Y_i^{(n)}, h^{(n)}]$. The first term on the right hand side (r.h.s.) represents the convective term while the second term, $\bar{\rho} S_{\alpha}^r(\phi^{(n)}) dt$, is due to the chemical reactions. The third term, $\bar{\rho} S_{\alpha}^s(\phi^{(n)}) dt$, is the source term due to the spray evaporation. This is different for each species, *i.e.*, solely the evaporating species is involved but it is identical for each stochastic field. The fourth term corresponds to a gradient transport model for turbulent velocity fluctuation, where $\Gamma_i = \mu_t / \sigma_i$ is the turbulent diffusivity. Here, μ_t is the turbulent viscosity while σ_i is the turbulent Schmidt number (Sc_i) in the transport equations for chemical species or the Prandtl number (Pr_i) in the enthalpy transport equation. Both Sc_i and Pr_i are set to 0.7 in the current work. The fifth term, which involves the mixing constant, C_{ϕ} , represents the molecular mixing. The mixing constant is fixed at $C_{\phi} = 2$. It is modelled using the Interaction with Exchange to the Mean model. ω_i therein is the turbulence frequency obtained from $\omega_i = \epsilon / k$ where k and ϵ are the turbulent kinetic energy and its dissipation rate, respectively. In the last term on the r.h.s., $dW^{(n)}$ represents a vector Wiener process that is spatially uniform but different for each field. The purpose of this term is to introduce a stochastic noise in the transport equations and generate consequent PDF for chemical species and enthalpy. In these simulations, $dW^{(n)}$ is represented by a time-step increment $\Delta t^{1/2} \eta_i^n$, where $\eta_i^n = \{-1, 1\}$ is a dichotomic random vector. Previous work has shown that the use of thirty-two stochastic fields reached result convergence [35]. The Chemistry Coordinate Mapping (CCM) approach is coupled with the ESF solver in order to integrate the chemical reaction source terms efficiently [36]. In the current work, a four-dimensional phase space based on temperature, local equivalence ratio, scalar dissipation rate, and the mass fraction of fuel is used. Their resolutions are fixed at 5 K, 0.01, 0.025 and 0.001, respectively. The ESF-CCM solver is incorporated with a revised multi-step soot model [14,20]. Mean molar concentrations of acetylene (C_2H_2) and O_2/OH are used to estimate the soot formation and oxidation rates, respectively. Both soot and gas radiation heat transfers are not considered in the current work. Bolla

et al. [37] showed that the effect of radiation heat transfer influences the local flame temperature in the order of $O(10\text{ K})$ and hence has minor influence on local NO and soot concentrations under the Spray A condition. While the effects of radiation heat transfer are more significant at higher P_{am} due to the increased concentrations of soot, CO_2 and H_2O , they may only vary the absolute values. Comparisons to the experimental results in Section 4 show variation of combustion and emissions characteristics with respect to the change of P_{am} levels are captured by the current model. These qualitative trends are expected to remain unchanged with the consideration of radiation heat transfer.

The computational domain is a constant volume chamber, which has a cubic shape with side lengths of 108 mm. The injector is placed at the center of one of the chamber walls. A uniform Cartesian grid is used. In the previous study, an isotropic cell size of 0.5 mm within the spray combustion region was found to reach mesh independence [35]. This mesh resolution is set as the baseline configuration and mesh sensitivity studies are carried out for different P_{am} in the current work. The computational grid with the fine, intermediate (baseline) and coarse resolutions consists of approximately 1,440,000, 360,000 and 89,000 cells, respectively. Fig. 3 shows that the penetration lengths and mixture fraction generated by the finer resolution and the baseline are close while those by the coarser resolution deviate, particularly for liquid fuel penetration length. It should also be mentioned that the qualitative change of the ignition behavior (see Section 4) with respect to the variation of P_{am} is also consistent when a finer resolution is used.

4. Results and discussion

4.1. Model validation

Fig. 4 depicts the temporal evolution of the liquid and vapor penetration lengths of the evaporating, non-reacting sprays from the experiments and the numerical models. The liquid penetration reaches steady state after 0.5 ms, while the vapor penetration continues to grow with time. The model is capable to replicate the experimental penetration lengths reasonably well. As the P_{am} increases and hence the ρ_{am} increases, both the liquid and vapor penetration lengths decrease due to the increased droplet drag caused by the higher ρ_{am} .

Model evaluation is performed further for evaporating, non-reacting sprays with D_{nozz} of 180 μm . Since experimental data are not available for D_{nozz} of 180 μm , model evaluation is carried out based on liquid scaling law [8] as well as dimensionless penetration length and time [9]. The current spray breakup model configuration is found applicable for both D_{nozz} of 180 and 257 μm , i.e., the same spray sub-model constants were used. Fig. 5 shows that the predicted liquid penetration

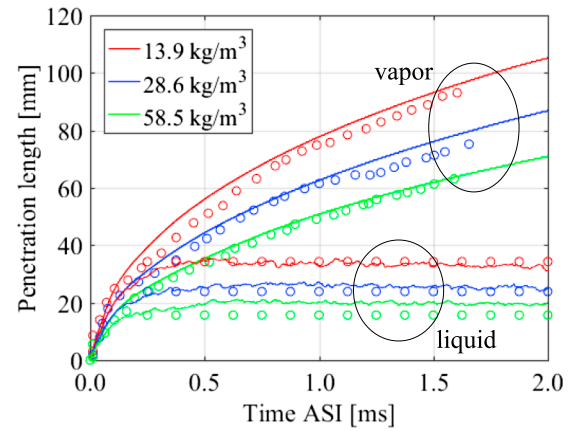


Fig. 4. Liquid and vapor penetration lengths of the evaporating, non-reacting sprays (cases 1–3) as a function of time after start of injection (ASI). Solid lines denote the simulation results while markers are obtained by liquid scaling law (liquid) [8] and from the experiment (vapor) [9].

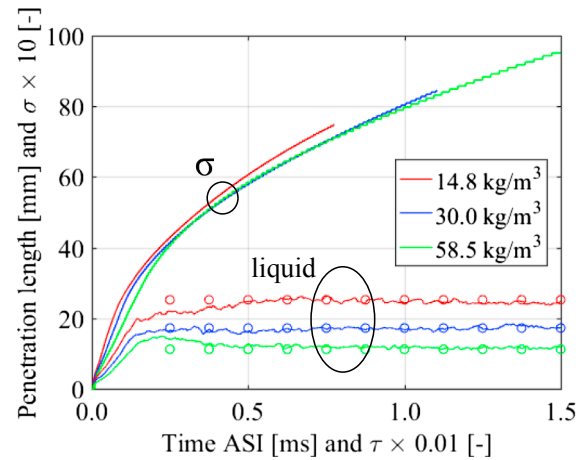


Fig. 5. Predictions of liquid penetration lengths and dimensionless penetration distance (σ) as a function of dimensionless penetration time (τ). Circle markers denote liquid scaling law results.

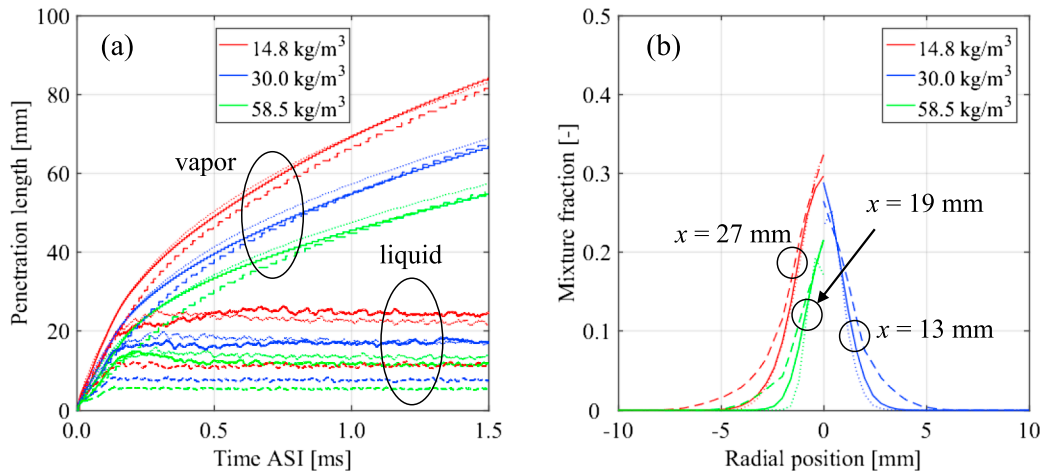


Fig. 3. (a) Penetration lengths and (b) mixture fraction distribution at axial position (x) near the end of liquid penetration length predicted using different mesh resolution. Dashed-, solid- and dotted-lines are results of the coarse, intermediate (baseline) and fine resolutions, respectively.

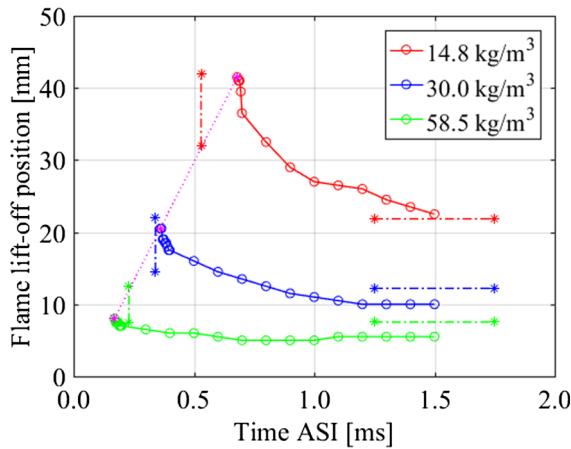


Fig. 6. Flame lift-off positions of the reacting sprays (cases 4–6) as a function of time after start of injection (ASI). Vertical and horizontal dash-dotted lines with asterisks represent the experimental ignition delay times and averaged flame lift-off lengths, respectively [3,10]. Magenta dotted line indicates the boundary separating the domain of ignition (larger time ASI) and induction to ignition (smaller time ASI).

in Fig. 5, all the σ curves collapse, agreeing well with the trend reported in [5]. This indicates that the dependence of vapor penetration length on ρ_{am} is successfully simulated by the model.

The decrease in both liquid and vapor penetration lengths lead to

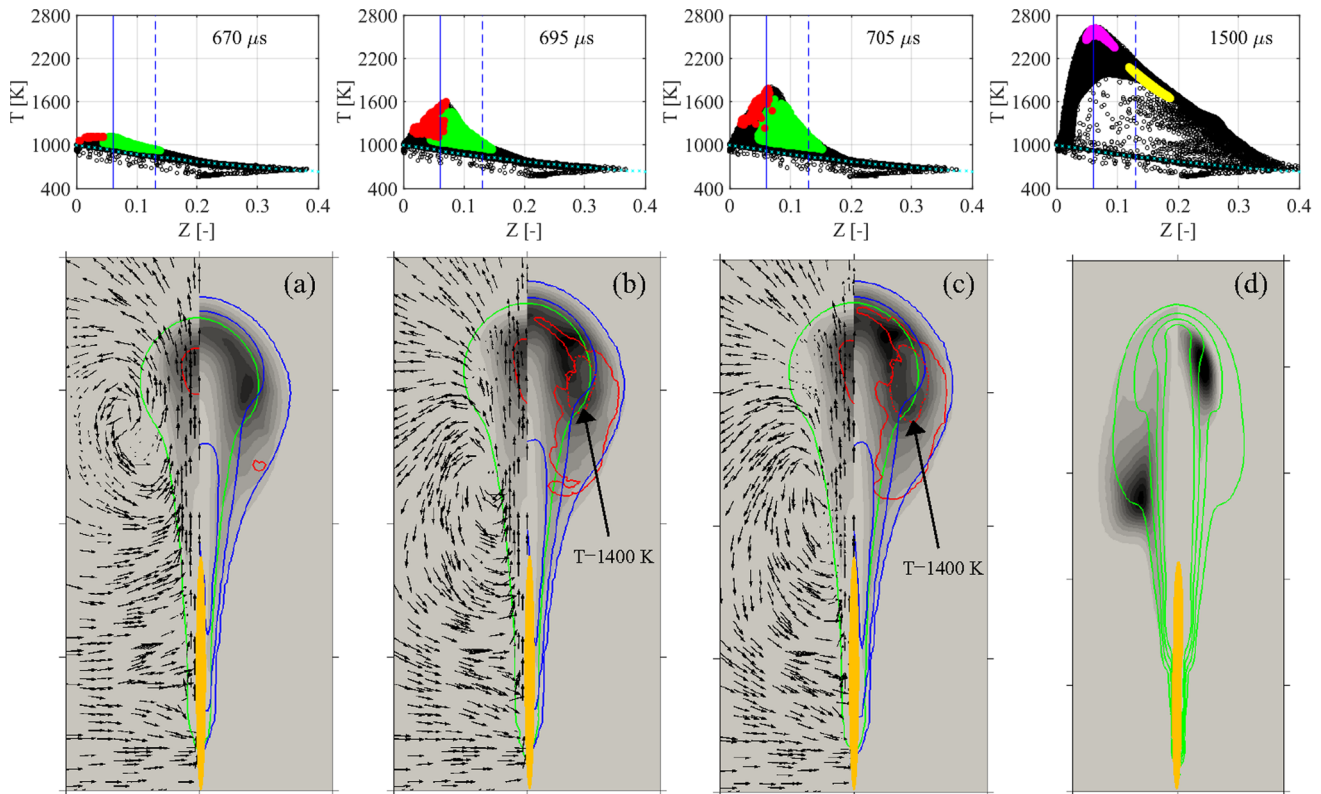


Fig. 7. Scatter plots of temperature-mixture fraction (upper row) and contours of combustion products (bottom row) in the 14.8 kg/m³ case a) at first-stage ignition, b) at onset of second-stage ignition, c) towards the formation of a classical diesel spray flame and d) during quasi-steady state. Upper row: Cells with substantial formation of HO₂, OH, NO and soot volume fraction ($f_{v,soot}$) are marked with green, red, magenta and yellow, respectively. The thresholds are set to 40% of their respective maximum mass fraction. Stoichiometric lines, the most reactive mixture fraction and mixing lines are represented by solid blue, dashed blue and dotted cyan lines respectively. Bottom row (a)–(c): (Left) Ketohydroperoxide contour with flowfield (black arrows), RO₂ of 1×10^{-4} (solid red); and (right) HO₂ contour with isolines of scalar dissipation rates of 1, 10 and 100 (solid blue), OH mass fraction of 1×10^{-4} (solid red), temperature of 1400 K (dotted red); (d) (Left) NO and (right) $f_{v,soot}$ contours at quasi-steady state with isolines of local equivalence ratio of 1–4 (solid green). Maximum mass fraction of ketohydroperoxide, HO₂, and NO is fixed at 0.03, 0.001 and 0.002 respectively while maximum soot volume fraction is set to 5 ppm. Solid green lines indicate the stoichiometric line and the orange lines represent the averaged liquid length. For (a) to (c), each frame shows 30 × 60 mm while for (d), the frame shows 40 × 100 mm.

the ignition site and the flame stabilization position to move upstream towards the injection tip, reducing the LOL (see Fig. 6). A comparison to the measurements shows that the IDTs and flame LOLs are predicted within 28% for all three cases. The difference is mainly attributed to the overestimated IDT in the 42 bar case. It is interesting to note that a similar simulation result was reported by Bolla et al. [17], when a different TCI closure approach, the conditional moment closure model, was employed with the same mechanism for the same thermochemical conditions. Although the IDTs and LOLs predicted are to a certain extent different from the experiment, the trend of IDT and LOL with respect to the change of P_{am} is correctly predicted.

4.2. Autoignition characteristics of diesel spray combustion

Figs. 7–9 illustrate the autoignition characteristics of the three cases using scatter plots of temperature (T)-mixture fraction (Z) and contours of various combustion products. In the 42 bar case, RO₂ is formed in the fuel-rich inner core of the spray jet with a temperature around 750 K, starting at approximately 350 μs (not shown). Through the low-temperature reaction pathway, RO₂ oxidizes to ketohydroperoxide. The HO₂ radical is formed in the vicinity of ketohydroperoxide, extending to the fuel-lean side of the stoichiometric line. These species are formed downstream of the liquid fuel. The first-stage ignition is found across a wide range of mixture fraction. As shown in Fig. 7(a), a small amount of OH is formed at 670 μs on the fuel-lean side and the peak temperature increases above 1100 K. Fig. 7(b) depicts that HO₂ reaches a higher concentration in the fuel-rich zone at 695 μs, as compared to that in the

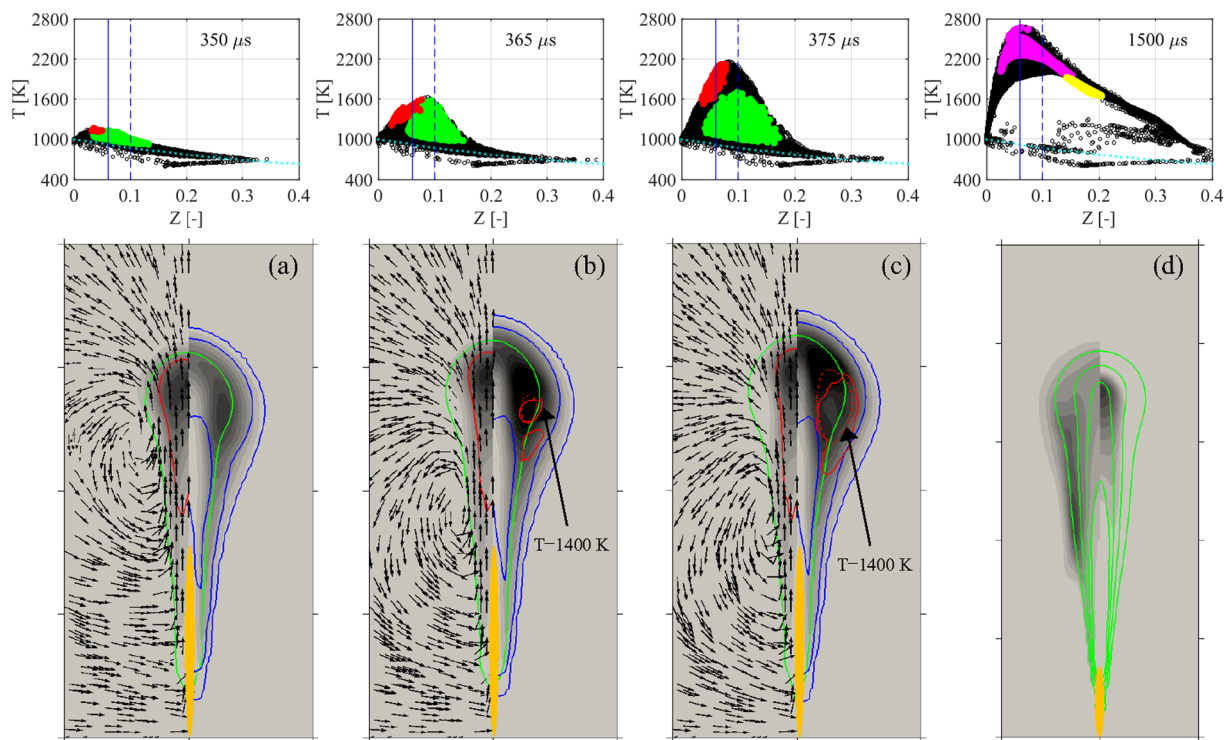


Fig. 8. Scatter plots of temperature-mixture fraction (upper row) and contours of combustion products (bottom row) in the 30.0 kg/m^3 case at different times. Descriptions can be found in the caption of Fig. 7, apart from maximum soot volume fraction which is set to 50 ppm. For (a)–(c), each frame shows $20 \times 40 \text{ mm}$ while for (d), the frame shows $40 \times 100 \text{ mm}$.

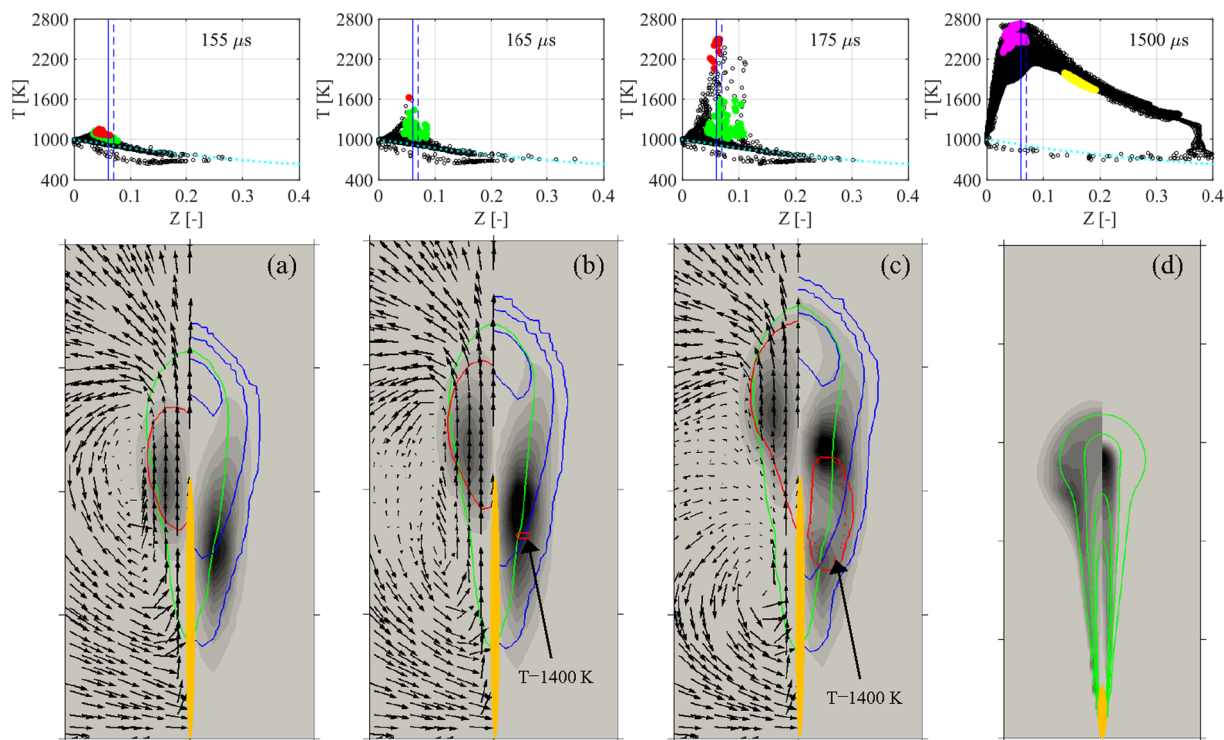


Fig. 9. Scatter plots of temperature-mixture fraction (upper row) and contours of combustion products (bottom row) in the 58.5 kg/m^3 case at different times. Descriptions can be found in the caption of Fig. 3, apart from maximum soot volume fraction which is set to 500 ppm. For (a)–(c), each frame shows $5 \times 20 \text{ mm}$ while for (d), the frame shows $40 \times 100 \text{ mm}$.

fuel-lean zone. HO_2 in this region is first consumed and OH is formed. The local temperature increases beyond the temperature threshold of 1400 K (400 K above T_{am}), indicating the onset of the main ignition. Rate of production (ROP) analysis of the 0-D simulation of Z_{mr} (in

Section 4.1) shows that OH is mainly formed from the sequence $\text{HO}_2 + \text{HO}_2 \rightleftharpoons \text{H}_2\text{O}_2 + \text{O}_2$ (R1), $\text{H}_2\text{O}_2 + M \rightleftharpoons 2\text{OH} + M$ (R2), where M is the third body species. It is also noticed that the main ignition occurs in the region where the scalar dissipation rate (χ) is low and the

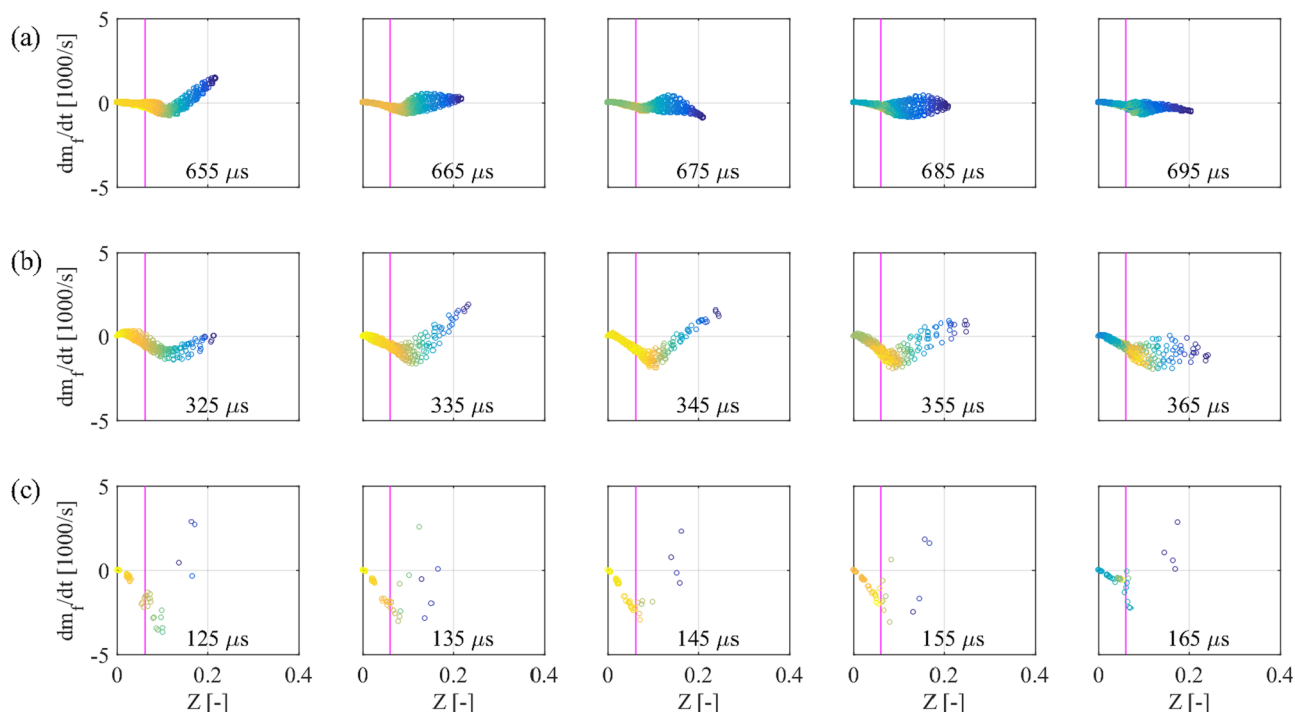


Fig. 10. Scatter plots of rate of fuel concentration change and mixture fraction for (a) the 14.8 kg/m³ case at 44 mm from the injector tip, (b) the 30.0 kg/m³ case at 26 mm from the injector tip and (c) the 58.5 kg/m³ case at 8 mm from the injector tip. The last column provides scatter plots at their respective main high temperature ignition.

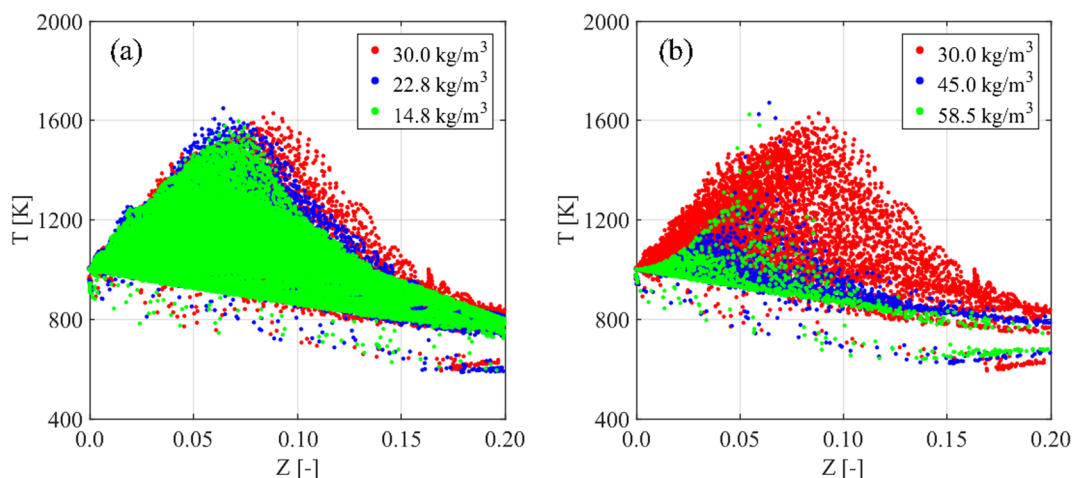


Fig. 11. Scatter plots of temperature-mixture fraction of (a) the 14.8 kg/m³ case at 695 μ s, the 22.8 kg/m³ case at 470 μ s, the 30.0 kg/m³ case at 365 μ s and (b) the 30.0 kg/m³ case at 365 μ s, the 45.0 kg/m³ case at 230 μ s and the 58.5 kg/m³ case at 165 μ s.

residence time is long (within the center of the recirculation zone).

The formation of RO₂, ketohydroperoxide and HO₂ starts earlier at approximately 200 μ s in the 85 bar case (not shown). Fig. 8(a) depicts that OH formation is formed at 350 μ s in the fuel-lean region where the local temperature exceeds 1100 K. The second-stage ignition then takes place at 365 μ s on the fuel-rich side of the stoichiometric line, in the region where χ is low and the residence time is long. These phenomena are akin to those of 42 bar case discussed above, although the transition from low- to high-temperature ignition has a shorter duration. A shorter transition is also observed in the homogenous reactor calculation (cf. Fig. 2). Reaction path analysis shows that reaction R(2) remains the most significant step during the main ignition event. When P_{am} increases, the separation between the end of liquid fuel and key radicals such as RO₂, ketohydroperoxide and HO₂ reduces. The ignition site is closer to the penetration tip where the local Z value is higher. In the 42

and 85 bar cases, the mixture on the fuel-lean side first experiences a higher temperature rise, presumably due to the higher T_{am} . It then promotes the low-temperature reactions in the rich mixture due to the transport of warmer lean products into the fuel-rich zone. These phenomena are similar to those reported in Refs. [4–7], which studied the ignition behavior for the Spray A condition ($O_{2,am} = 15\%$; $T_{am} = 900$ K; $P_{am} = 60$ bar). The observation that the main ignition event occurs in more fuel-rich mixtures in the case with higher P_{am} is consistent with the findings of Higgins et al. [12] who experimentally studied the ignition behavior at different ρ_{am} in the same combustion vessel. However, the behavior changes when P_{am} is further increased. As discussed next, the current results show that the mixture fraction of the first igniting mixture during the high-temperature ignition does not vary monotonically with P_{am} and the second-stage ignition takes place in a more fuel-lean region in the 170 bar case.

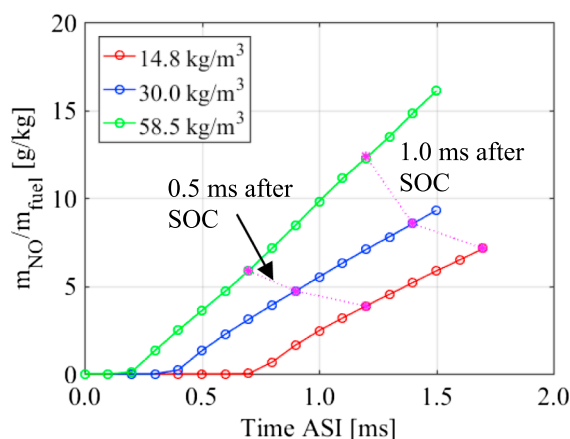


Fig. 12. Normalized total mass of NO as a function of time after injection (ASI). Magenta dotted lines indicate the total NO mass production remains higher after their respective start of combustion (SOC).

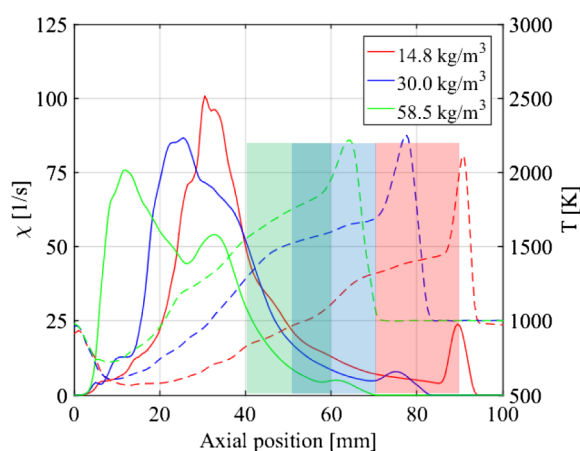


Fig. 13. Scalar dissipation rate, χ (solid lines) and temperature (dashed lines) along the spray axis. Semi-transparent windows indicate the domains with high soot volume fraction as can be seen in Figs. 7–9.

At 170 bar, RO_2 , ketohydroperoxide and HO_2 are formed early at 100 μs (not shown). The temperature of the fuel-lean mixture increases to above 1100 K at 150 μs . Under this condition, the transition from low- to high-temperature ignition is even faster, occurring in less than 15 μs . The transport of warmer products from the fuel-lean zone into the fuel-rich mixture is relatively slow, as compared to the increased reaction rate. Fig. 9 depicts that there is no separation in the spray direction between HO_2 and liquid fuel, i.e., HO_2 is formed in the vicinity of the fuel spray region. Within the fuel-rich region, the local temperature is low due to evaporation and the condition is not appropriate for ignition. The scatter plots in Figs. 8(b) and 9(b) support that, during the high-temperature ignition, the local temperature within the fuel-rich region becomes lower when P_{am} increases. Eventually, the high-temperature ignition occurs on the fuel-lean side of the stoichiometric line.

The ignition characteristics from low- to high-temperature ignition in the three cases are also illustrated using the scatter plots of rate of fuel concentration change and mixture fraction on the horizontal plane where their respective ignition occurs. These plots can be found in Fig. 10. A positive value indicates the presence of vapor fuel while a negative value denotes the fuel consumption. Each plot is colored by the normalized local temperature at that particular timestep, i.e., dark blue, blue, green and yellow indicate low, intermediate, high, the highest temperature, respectively. The magenta vertical line represents the stoichiometric line. At 42 and 85 bar, the higher temperature

regime first falls on the fuel-lean mixture and then shifts to the fuel-rich mixture. During the main ignition process, the fuel has been consumed where the main ignition event occurs. On the other hand, at 170 bar, the vapor fuel is still observed but the corresponding mixture is cold and does not get involved in the ignition process. The mixture on the fuel-lean side of the stoichiometric line undergoes low- and then high-temperature ignition. These support the discussion earlier based on Figs. 7–9.

Computation of two additional intermediate cases of ρ_{am} of 22.8 kg/m³ (67 bar) and 45.0 kg/m³ (128 bar) confirms this trend. Fig. 11 demonstrates that the main ignition occurs in more fuel-rich mixtures when P_{am} increases from 42 bar to 85 bar, consistent with results of Higgins et al. [12]. Above 85 bar, the mixture that undergoes the main ignition becomes more fuel-lean when P_{am} increases. In order to further verify this trend, simulations are performed using the Lu68 mechanism [16] for cases 5 and 6. The predicted IDT using the Lu68 mechanism is slightly closer to the measurement in the 170 bar case (case 6), with a relative difference of > 8% from the measurement, as compared to that using the Liu44 mechanism with a relative difference of ~10% from the measurement. The high-temperature ignition occurs on the fuel-rich side (Z of 0.109) and the fuel-lean side (Z of 0.0603) in the 85 bar (case 5) and 170 bar (case 6), respectively, showing that the qualitative change of the ignition behavior with respect to the variation of P_{am} from 85 bar to 170 bar is the same for the Liu44 and Lu68 mechanisms. It should be noted that the variation of Z of the first ignition mixtures during the high-temperature ignition is identified for these particular injection specifications, initial ambient gas composition and T_{am} . As the ignition behavior is dependent of both physical and chemical processes, the variation of Z of the first ignition mixtures during the high-temperature ignition with respect to P_{am} may change. Understanding the ignition behavior is crucial for development of skeletal surrogate fuel mechanisms. Once the ignition behavior is identified for a narrower range of operating conditions, the size of the skeletal surrogate fuel mechanisms can be further optimized to increase the computational efficiency.

Effects of P_{am} on the quasi-steady state flame structures will be discussed next. Upon the ignition point, it takes approximately 160 h for 0.1 ms on ten 64-bit Intel Ivy Bridge Xeon E5-2650 v2 8-core CPUs running at 2.60 GHz with the Liu44 mechanism. The computational cost is expected to escalate significantly with the use of the Lu68 mechanism. Hence, only the Liu44 mechanism is used for the simulations up to quasi-steady state and the associated results are used for the flame structure analyses.

4.3. Quasi-steady state

An analysis based on transport budgets [38] near the lift-off position at quasi-steady state suggests the flame is stabilized by the auto-ignition process. This remains unchanged for three P_{am} levels and agrees with the findings from the literature. In addition to that, the Takeno's flame index (FI) is used to investigate the spray flame structure [39]. The local equivalence ratio is incorporated into FI such that the premixed flame can be identified for both fuel-lean and fuel-rich conditions, as shown in Eq. (2),

$$FI = \frac{\nabla Y_F \cdot \nabla Y_O}{|\nabla Y_F \cdot \nabla Y_O|} \cdot \frac{\phi - 1}{|\phi - 1|} \quad (2)$$

where the mass fraction of fuel, Y_F includes those of evaporating species, n -heptane as well as the main fuel-rich combustion products, i.e. CO and H_2 [35]. The quasi-steady spray structures are found independent from the effects of P_{am} at the tested initial T_{am} and ambient gas composition. Takeno's FI shows that all the spray flames have the classical structure of the diesel spray flames described in the Dec conceptual model, i.e., a premixed rich flame upstream embedded by a diffusion flame which extends downstream [40]. Figs. 7(d), 8(d) and 9(d) demonstrate that the location of NO and soot formation regions for

the three P_{am} levels. High NO concentration is found above 2200 K near the stoichiometric mixture, while high soot concentration is in the premixed fuel-rich zone with local temperature ranging from 1600 to 2200 K; this result is consistent with the literature [40,41]. A decrease in the flame size (in terms of both flame length and width) with the increase of P_{am} can also be seen in Figs. 7(d), 8(d) and 9(d). An evaluation of the reaction zone thickness based on the full-width at half maximum of OH mass fraction at the middle of the spray flames shows that the thickness of the reaction zone is approximately 7.2, 3.2 and 1.6 mm for the 14.8, 30.0 and 58.5 kg/m³ cases, respectively. These trends are in qualitative agreement with the experimental images based on OH chemiluminescence [11]. The reaction zone thickness for the O radicals exhibits a similar trend as those of OH. The spatial NO distribution becomes narrower when P_{am} increases. Although the reaction zone size decreases with the increasing ambient pressure, the rate of NO formation increases more rapidly with increasing P_{am} . The increased reaction rate attributed by the increased P_{am} is more influential to the final NO production. The total NO formation hence increases with P_{am} , as indicated by the magenta dotted lines in Fig. 12. The current model predicts that the peak soot volume fraction ($f_{v,soot}$) increases approximately six-fold when P_{am} increases from 42 to 85 bar and further increases approximately thirteen-fold when P_{am} further increases from 85 to 170 bar. To date, the revised multi-step model has only been evaluated using $f_{v,soot}$ measurements collected at 42 and 85 bar [14,20] since $f_{v,soot}$ measurement above 85 bar is not available. Further work is thus required to confirm the estimation of $f_{v,soot}$ at 170 bar. Yet, the trend of maximum $f_{v,soot}$ increasing with P_{am} agrees with experimental observations [13].

Fig. 2 shown earlier illustrates that the ignition site is placed further upstream and the flame stabilizes more quickly when P_{am} increases. At quasi-steady state, the flame LOL reduces with increasing P_{am} . This reduces the air entrainment, giving rise to a higher mixture fraction within the fuel-rich core region. Besides that, the elevated reaction rate at higher P_{am} also promotes soot formation. These factors are known to increase the local peak $f_{v,soot}$ [13]. The current study shows that the rise of the soot formation rates can be attributed to other factors. As aforementioned, the flame width reduces for a higher P_{am} . Consequently, the stoichiometric line or the mixing-controlled combustion layer is closer to the central region with higher P_{am} , which increases the heat transfer. As shown in Fig. 13, the temperature in the rich premixed region increases with P_{am} , contributing to the higher soot formation rates. Apart from these, it is noticed that both the velocity near the spray region and χ decrease with the rise of P_{am} . This indicates the mixing rate within the fuel-rich region decreases, promoting soot precursor and particle formation within the fuel-rich region. These collectively contribute to the higher local $f_{v,soot}$ when P_{am} increases.

5. Concluding remarks

The contribution of this study is the generalization of the ignition behaviors and flame structures at different ambient pressures (P_{am}) under diesel engine-like conditions. Diesel #2 spray flames at three P_{am} levels of 42, 85 and 170 bar have been studied using an Eulerian-based transported probability density function model in three-dimensional computational fluid dynamic simulations. Comparisons to measurements show that the ignition delay times and flame lift-off lengths are predicted fairly well. The numerical results show that the mixture fraction of the first igniting mixture during the high-temperature ignition does not vary monotonically with P_{am} . The high-temperature ignition takes place on the fuel-rich side in the 42 bar and 85 bar cases. However, at 170 bar the high-temperature ignition occurs on the fuel-lean side due to the increased reaction rates and temperature in the fuel-lean mixture. The main ignition in all three cases occurs in the region where the scalar dissipation rate (χ) is low and the residence time is long. Analyses of the quasi-steady spray flame structures reveal that the stoichiometric mixtures are closer to the fuel-rich core when

P_{am} is increased, leading to higher heat transfer and increased temperature within the fuel-rich core. Besides that, χ reduces in cases with higher P_{am} . These collectively contribute to the higher local soot volume fraction when P_{am} increases, in addition to poorer air entrainment attributed by the reduced lift-off length and the increased reaction rates.

Acknowledgements

The authors gratefully acknowledge the financial support from the Innovation Fund Denmark and MAN Energy Solutions through the SULCOR project. The computation was performed using the Niflheim cluster at Technical University of Denmark.

References

- [1] Hult J, Matlok S, Mayer S. Particle image velocimetry measurements of swirl and scavenging in a large marine two-stroke diesel engine. SAE paper 2014;2014-01-1173.
- [2] Hult J, Matlok S, Mayer S. Optical diagnostics of fuel injection and ignition in a marine two-stroke diesel engine. SAE Int J Engine 2014;7: 2014-01-1448.
- [3] Engine Combustion Department of Sandia National Laboratories. Engine Combustion Network. Available at < <http://www.sandia.gov/ecn/> > [accessed 17.12.2017].
- [4] Krisman A, Hawkes ER, Talei M, Bhagatwalaa A, Chen JH. A direct numerical simulation of cool-flame affected autoignition in diesel engine-relevant conditions. Proc Combust Inst 2017;36:3567–75.
- [5] Dahms RN, Paczko GA, Skeen SA, Pickett LM. Understanding the ignition mechanism of high-pressure spray flames. Proc Combust Inst 2017;36:2615–23.
- [6] Kundu P, Ameen MM, Som S. Importance of turbulence-chemistry interactions at low temperature engine conditions. Combust Flame 2017;183:283–98.
- [7] Pei Y, Hawkes ER, Bolla M, Kook S, Goldin GM, Yang Y, et al. An analysis of the structure of an n-dodecane spray flame using TPDF modelling. Combust Flame 2016;168:420–35.
- [8] Siebers DL. Scaling liquid-phase fuel penetration in diesel sprays based on mixing-limited vaporization. SAE Paper 1999;1999-01-0528.
- [9] Naber JD, Siebers DL. Effects of gas density and vaporization on penetration and dispersion of diesel sprays. SAE Paper 1996;960034.
- [10] Siebers D, Higgins B. Flame lift-off on direct-injection diesel sprays under quiescent conditions. SAE Paper 2001;2001-01-0531.
- [11] Pickett LM, Siebers DL. Orifice diameter effects on diesel fuel jet flame structure. J Eng Gas Turbines Power 2005;127:187–96.
- [12] Higgins B, Siebers D, Aradi A. Diesel-spray ignition and premixed-burn behavior. SAE Paper 2000;2000-01-0940.
- [13] Pickett LM, Siebers DL. Soot in diesel fuel jets: effects of ambient temperature, ambient density, and injection pressure. Combust Flame 2004;138:114–35.
- [14] Pang KM, Karvounis N, Walther JH, Schramm J. Numerical investigation of soot formation and oxidation processes under large two-stroke marine diesel engine-like conditions using integrated CFD-chemical kinetics. Appl Energy 2016;169:874–87.
- [15] Pang KM, Karvounis N, Walther JH, Schramm J, Glarborg P, Mayer S. Modelling of temporal and spatial evolution of sulphur oxides and sulphuric acid under large, two-stroke marine engine-like conditions using integrated CFD-chemical kinetics. Appl Energy 2017;193:60–73.
- [16] Som S, Aggarwal SK. Effects of primary breakup modeling on spray and combustion characteristics of compression ignition engines. Combust Flame 2010;157:1179–93.
- [17] Bolla M, Gudmundsson T, Wright YM, Boulouchos K. Simulations of diesel sprays using the conditional moment closure model. SAE Int J Engine 2013;6:1249–61.
- [18] Valino L. A field monte carlo formulation for calculating the probability density function of a single scalar in a turbulent flow. Flow Turb Combust 1998;60:157–72.
- [19] Liu S, Hewson JC, Chen JH, Pitsch H. Effects of strain rate on high-pressure non-premixed n-heptane autoignition in counterflow. Combust Flame 2004;137:320–39.
- [20] Pang KM, Jangi M, Bai X-S, Schramm J. Evaluation and optimisation of phenomenological multi-step soot model for spray combustion under diesel engine-like operating conditions. Combust Theor Model 2015;19:279–308.
- [21] Hashemi H, Christensen JM, Gersen S, Levinsky H, Klippenstein SJ, Glarborg P. High-pressure oxidation of methane. Combust Flame 2016;172:349–64.
- [22] Hashemi H, Jacobsen JG, Rasmussen CT, Christensen JM, Glarborg P, Gersen S, et al. High-pressure oxidation of ethane. Combust Flame 2017;182:155–60.
- [23] Hashemi H, Christensen JM, Harding LB, Klippenstein SJ, Glarborg P. High-pressure oxidation of propane. Proc Combust Inst 2018. <https://doi.org/10.1016/j.proci.2018.07.009>.
- [24] Mehl M, Pitz WJ, Westbrook CK, Curran HJ. Kinetic modeling of gasoline surrogate components and mixtures under engine conditions. Proc Combust Inst 2011;193–200.
- [25] Lu T, Law CK. Strategies for mechanism reduction for large hydrocarbon: n-heptane. Combust Flame 2008;154:153–63.
- [26] Zhang K, Banyon C, Bugler J, Curran HJ, Rodriguez A, Herbinet O, et al. An updated experimental and kinetic modeling study of n-heptane oxidation. Combust Flame 2016;172:116–35.
- [27] Pei Y, Liu W, Mehl M, Som S, Lu T, Pitz WJ. A multicomponent blend as a diesel fuel surrogate for compression ignition engine applications. J Eng Gas Turbines Power

- 2005;137:Paper GTP-15-1057.
- [28] Poon HM, Pang KM, Ng HK, Gan S, Schramm J. Development of multi-component diesel surrogate fuel models. Part II: validation of the integrated mechanisms in 0-D kinetic and 2-D CFD spray combustion simulations. *Fuel* 2016;181:120–30.
- [29] Anon. CHEMKIN-PRO software: theory manual. Reaction Des 2008.
- [30] Mastorakos E, Baritaud TA, Poinot TJ. Numerical simulations of autoignition in turbulent mixing flows. *Combust Flame* 1997;109:198–223.
- [31] Mastorakos E. Ignition of turbulent non-premixed flames. *Prog Energy Combust Sci* 2011;35:57–97.
- [32] Pei Y, Hawkes ER, Kook S. A comprehensive study of effects of mixing and chemical kinetic models on predictions of n-heptane jet ignitions with the PDF method. *Flow Turbul Combust* 2013;91:249–80.
- [33] The OpenFOAM Foundation. 2015. Available at < www.openfoam.org/ > [accessed 08.09.2016].
- [34] Easley W, Mellor A. NO decomposition in diesel engines. SAE Paper 1999;1999-01-3546.
- [35] Pang KM, Jangi M, Bai X-S, Schramm J, Walther JH. Modelling of ignition and flame lift off using an accelerated Eulerian stochastic fields method. *Combust Flame* 2018;193C:363–83.
- [36] Jangi M, Lucchini T, Gong C, Bai X-S. Effects of fuel cetane number on the structure of diesel spray combustion: an accelerated Eulerian stochastic fields method. *Combust Theor Model* 2015;19:549–67.
- [37] Bolla M, Chishty MA, Hawkes ER, Chan NQ, Kook S. Influence of turbulent fluctuations on radiation heat transfer, NO and soot formation under ECN Spray A conditions. *Proc Combust Inst* 2017;36:3551–8.
- [38] Gordon RL, Masri AR, Pope SB, Goldin GM. Transport budgets in turbulent lifted flames of methane autoigniting in a vitiated co-flow. *Combust Flame* 2007;151:495–511.
- [39] Mizobuchi Y, Tachibana S, Shinio J, Ogawa S, Takeno T. A numerical analysis of the structure of a turbulent hydrogen jet lifted flame. *Proc Combust Inst* 2002;29:2009–15.
- [40] Dec JE. A conceptual model of DI diesel combustion based on laser-sheet imaging. SAE Paper 1997;970873.
- [41] Flynn PF, Durrett RP, Hunter GL, zur Loye AO, Akinyemi OC, Dec JE, Westbrook CK. Diesel combustion: an integrated view combining laser diagnostics, chemical kinetics, and empirical validation. SAE Trans 1999;108:587–600.